Thermal decomposition kinetics of $FAPbI_3$ thin films

Thomas Burwig [*] and Karl Heinze
Martin Luther University Halle-Wittenberg, Von-Danckelmann-Platz 3, 06120 Halle (Saale), Germany

Paul Pistor [†]
Martin Luther University Halle-Wittenberg, Von-Danckelmann-Platz 3, 06120 Halle (Saale), Germany and Universidad Pablo de Olavide, Carretera de Utrera 1, 41013 Sevilla, Spain

(Received 7 February 2022; accepted 3 June 2022; published 27 June 2022)

In the realm of organic-inorganic-hybrid metal-halide perovskites, $FAPbI_3$ is seeing increasing attention as a potentially more stable alternative to $MAPbI_3$. To add to our previous paper, where we studied the reaction kinetics of the thermal decomposition of $MAPbI_3$, here we analyze the compositional change and crystal phase evolution during the thermal decomposition of $FAPbI_3$ thin films. To this end, we prepare the perovskite using thermal coevaporation and monitor the growth and thermal decomposition in vacuum with an *in situ* x-ray diffraction setup. The experimental procedure has been carried out via three approaches: producing a partially decomposed sample with the help of a graded temperature profile, using a temperature ramp and a set of isothermal decomposition experiments. From this data we analyze and calculate the stoichiometry and phase changes, the activation energy E and the frequency factor A of the thermal decomposition process, in addition to the thermal expansion coefficient during heating. We compare our results to the ones obtained for $MAPbI_3$ thin films by the same experimental method, confirming the enhanced thermal stability of $FAPbI_3$.

DOI: 10.1103/PhysRevMaterials.6.065404

I. INTRODUCTION

Since the first successful demonstration of metal-halide perovskites as photoabsorbers in 2009 [1], this organic-inorganic semiconductor family has gained a lot of interest for a variety of applications, which, besides photovoltaics, include high energy photon detectors [2,3], LEDs [4–7], and lasers [8]. In all of these applications, metal-halide perovskites, such as the prototypical methyl ammonium lead iodide ($MAPbI_3$) and derivatives based on Cs, formamidinium (FA), Sn, Br, or Cl, have shown significant potential for enabling efficient, low-cost optoelectronic devices. The most significant drawback of these perovskite-based devices, however, is their lack of stability towards a variety of environmental factors such as heat, moisture, or UV illumination [9]. In this paper we will focus on thermal stability aspects and the decomposition kinetics of the perovskite absorber formamidinium lead iodide $FAPbI_3$, complementing our previous paper on $MAPbI_3$ [10].

Solar cells can reach up to 85 °C under operating conditions [11] and, in contrast to moisture-related degradation, thermal decomposition cannot be alleviated by encapsulation. Therefore it is vital to understand the thermal decomposition pathways and kinetics for these materials in view of any application where the material is subjected to heat. For the workhorse material $MAPbI_3$ it has become clear that severe degradation may occur at comparatively low temperatures, close to the operating conditions of solar cells, while the exact onset of degradation is still a matter of dispute [12]. This uncertainty applies even more so to the recently strongly investigated perovskite $FAPbI_3$, where less stability studies are available. As Zhang *et al.* point out, the observed decomposition depends significantly on the chosen temperature regime, as isothermal experiments usually found decompositions at much lower temperatures than ramp experiments [12]. Our earlier results on the thermal stability of $MAPbI_3$, using a temperature ramp, showed a 50 % decomposition at 230 °C [13] and Dualeh *et al.* found an onset of the decomposition of $MAPbI_3$ at 234 °C, again using a temperature ramp [14]. In contrast to this, Kim *et al.* have found a detectable decomposition of $MAPbI_3$ at 80 °C after 1 h [15]. This conflict is an example for one of several problems, which impede the formation of a complete and clear picture of the degradation mechanisms in current research: (i) As already noted, the choice of temperature regime significantly affects results. (ii) Degradation studies of completed solar cells often report only the decline in performance over time for a given temperature, lacking substantial information on the exact degree of decomposition. (iii) Many studies analyzing perovskite decomposition only report the degree of decomposition for one set of time and temperature, which does not allow for the extraction of kinetic parameters. This can also lead to difficulties when comparing the results of different research groups, especially when different conditions (e.g., different temperatures) are chosen for the trials. (iv) Materials with different morphologies (single crystal, powder, thin film) can be expected to degrade differently [16]. (v) The synthesis method can play a significant role in the stability of the resulting material. For example, solvent residues that remain after wet chemical preparation can decrease the stability [17]. (vi) The

[*] thomas.burwig@physik.uni-halle.de
[†] paul.pistor@physik.uni-halle.de

history of the investigated samples cannot be excluded as a factor for their stability. Samples that have been exposed to air (and thus to moisture, light, etc.) can reasonably be expected to show a different decomposition behavior. (vii) When temporarily exposing the samples to environmental factors, such as ambient air or light, these factors are often difficult to precisely quantify or are often not seen as "report-worthy" by the researchers.

It is for these reasons that in the current study we explicitly investigate thin films with properties similar to those applied in solar cells (e.g., in regard to thickness), that were prepared solvent-free in vacuum by coevaporation and investigated *in situ* within the vacuum chamber without air exposure at any time.

In the past, we have reported the synthesis, phase evolution and thermal decomposition of a variety of different perovskite thin films that were prepared by coevaporation in vacuum and studied via temperature ramp experiments with *in situ* x-ray diffraction (XRD) analysis. The materials studied so far include $MAPbI_3$, $MAPbBr_3$, $MAPbCl_3$ [13], $CsPbI_3$, $CsPbBr_3$ [18], and also the double perovskite $Cs_2AgBiBr_6$ [19,20]. To add to this list, $FAPbI_3$ will be studied in this paper.

While single temperature ramp experiments give a general idea of the thermal stability limits of a material and allow for a qualitative comparison of different materials, for a more detailed and general view of the decomposition kinetics, sets of isothermal measurements or sets of different temperature ramps are needed. In a previous paper, we elaborated on the kinetics of the thermal decomposition of $MAPbI_3$ in detail, by determining the kinetic triplet of this reaction. This consists of the activation energy E, the frequency factor A, and the reaction model $f(\alpha)$, where α is the extent of reaction [10]. These kinetic parameters allow for a generalization of the decomposition behavior over a larger temperature range and for more meaningful comparisons to other experiments. It has been shown by a large number of studies, that the major limiting component for the thermal stability of $MAPbI_3$ is the organic MA molecule [13,18,21–30]. Therefore, we study the impact of exchanging the MA molecule with FA to see how this modification influences the thermal stability of the resulting material. Solar cells that use $FAPbI_3$ absorber layers have been shown to be more resilient towards temperature [31] and moisture [32], which makes this material a promising object of study.

To our knowledge, there are three research groups that have investigated the reaction kinetics of the thermal decomposition of $FAPbI_3$: Juarez-Perez *et al.* used a wet-chemically prepared powder in vacuum and He atmosphere [33]. Pool *et al.* used spin coated thin films that were annealed under N_2 atmosphere [34]. Luongo *et al.* prepared a powder via dry grinding of the precursors and heated the samples up in Ar and He [35]. All of these trials use multiple temperature ramps to determine the kinetic data of the reaction and none of them use preparation methods that are likely candidates for use in industrial applications. Our goal is to complement these findings with isothermally acquired data on coevaporated thin films. The different preparation methods, experimental parameters and resulting values for E and A are compiled in Table III.

In order to be comparable to our previous experiments on the MA based perovskites [13], we first prepare $FAPbI_3$ in high vacuum via coevaporation of FAI and PbI_2. With an *in situ* x-ray diffraction setup, we are able to monitor the crystallization and phase evolution of the thin films at any time of the experiment. Afterwards, without breaking the vacuum, we perform three sets of decomposition measurements. First, a sample is decomposed using a temperature ramp in order to determine the general temperature range where a measurable decomposition is to be expected. In addition, we decompose $FAPbI_3$ thin films using a set of isothermal experiments in the temperature range between 230 °C and 290 °C. From this data we calculate the activation energy E and the frequency factor A for this process. The data is first analyzed under the assumption of a first-order model, where the rate constants k are determined by fitting an exponential decay onto the data. Then a more general approach is used, where the data is tested against a variety of different reaction models. Finally, we partially decompose a $FAPbI_3$ sample by applying a temperature gradient over the length of the sample, enabling us to investigate the morphology and stoichiometry changes during the decomposition via scanning electron microscopy (SEM) and energy-dispersive x-ray spectroscopy (EDX).

II. THEORY

A. $FAPbI_3$ crystal structure

Similarly to $CsPbI_3$, $FAPbI_3$ is a polymorph and can exist in different crystal phases at room temperature. The black, photoactive α phase has a band gap of 1.48 eV [31] and is sometimes identified with a cubic symmetry [$Pm3m$, $a = b = c = 6.3620(8)$ Å] [36], while other reports assign a trigonal symmetry [$P3m1$, $a = b = 8.9817(13)$ Å, $c = 11.006(2)$ Å] [37]. The δ phase is photo inactive, orange in appearance, has a band gap of 2.14 eV [38] and has a hexagonal crystal structure [$P6_3mc$, $a = b = 8.6603(14)$ Å, $c = 7.9022(6)$ Å] [37]. The α phase is stable for temperatures above 130 °C, while at lower temperatures the perovskite will gradually transform into the δ phase, even in an inert gas atmosphere [38,39]. A partial exchange of FA with MA [39] or of I with Br [40] has been shown to increase the stability of the photoactive α phase under ambient conditions.

B. Reaction kinetics

In general, the extent of conversion α of a reaction changes over the time t according to the following formula [41]:

$$\frac{d\alpha}{dt} = k(T)f(\alpha) \tag{1}$$

Here, T is the absolute temperature, k is the reaction rate and $f(\alpha)$ is the reaction model. α is defined as being 0 at the start of the reaction and 1 at the end. The data presented in this paper is tested against the same models as the $MAPbI_3$ samples in our previous work in Ref. [10]. The complete list of tested reaction models can be found in the Supplemental Material [42]. The selection of models was taken from Ref. [43], which also goes into detail about how these models are derived. The reaction rate $k(T)$ is defined as [41]:

$$k(T) = A\exp\left(-\frac{E}{RT}\right), \tag{2}$$

where R is the universal gas constant, E is the activation energy, and A is the pre-exponential factor. In principle, the kinetic parameters of a thermal decomposition reaction can be determined by a single temperature ramp experiment. However, as has been explained by Vyazovkin *et al.*, an experiment that uses a temperature ramp changes T and α simultaneously, which leads to a very high uncertainty in any determined kinetic parameters. If only a single temperature ramp experiment is used, this makes the results next to unusable [41]. For this reason, we use four isothermal experiments with different temperatures to determine the kinetic parameters of the degradation. For the first evaluation approach, we assumed the reaction model to be of first order, where an equation of the form

$$y = a\mathrm{e}^{-kx} \tag{3}$$

is fitted onto the data. Then $\ln k$ is plotted over $1/T$ for each isothermal experiment. An equivalent form of Eq. (2) is:

$$\ln k = \ln A - \frac{E}{RT}. \tag{4}$$

This has the same structure as the equation:

$$y = m + nx. \tag{5}$$

Therefore, a linear fit of the data for $y = \ln k$ over $x = 1/T$ can then be identified with this equation, which allows the calculation of $\ln A = m$ and $E = -nR$.

The second evaluation method used to analyze the kinetic data was a model fitting approach, which includes a variety of common reaction models. For this, different integrated reaction models $g(\alpha)$ are used, where $g(\alpha)$ follows from the reaction model $f(\alpha)$ by integration [41]:

$$g(\alpha) = \int_0^\alpha [f(\alpha)]^{-1}. \tag{6}$$

$g(\alpha)$ gives a unitless measure for the time it takes for the reaction to achieve a certain extend of conversion and, in this way, it relates the time t with the reaction rate $k(T)$ [41]:

$$g(\alpha) = k(T) \cdot t. \tag{7}$$

A plot of $g(\alpha)$ over t can be linearly fitted to yield a value for $k(T)$. Then, similarly to the first approach, $\ln k$ can then be plotted over $1/T$ and the kinetic parameters can be determined using an Arrhenius fit.

In our analysis, the peak area evolution of certain characteristic XRD peaks is assumed to be proportional to the amount of a given material within the film. The validity of this assumption has been discussed at length in our previous paper [10], and we only summarize the main points here. Besides a decomposition of the material, there are two main effects that could reduce the area of the detected peaks:

A layer of product (PbI_2) covers the film and reduces the detected x-ray intensity. To calculate the absorption B of a layer of PbI_2 with linear attenuation coefficient μ, coverage c, and thickness d when hit by x-rays with an incidence angle of θ, one can use the following formula:

$$B = c(1 - \mathrm{e}^{-\mu x}) \tag{8}$$

where $x = 2d/\sin\theta$ is the distance the x-rays travel through the film. To make an assessment as to the value of these parameters, the SEM images of the partial decomposition experiment, which are shown in Figs. 4 and 5, can be helpful to consider. Figure 5(d) shows an image with material contrast and, as can be seen there, the PbI_2 does not form a solid layer on top of the perovskite, but has a coverage of roughly 50 %. The cross-sectional image in Fig. 4(d) indicates a PbI_2 thickness of around 100 nm. The attenuation coefficient of PbI_2 for x-rays with an energy of 8.04 keV is 1556.51 cm^{-1} [44]. With the above mentioned values this would lead to an absorption of $B = 4.4\,\%$. This in itself can be considered negligible. While it is difficult to assess which extent of conversion corresponds to the SEM images, there is no PbI_2 at the beginning, therefore at $\alpha = 0$ the absorption is be $B = 0\,\%$. Since the evaluation of the isothermal experiments focuses on the first half of the decomposition, the impact of the PbI_2 absorption should be very limited. Additionally, the results for E and A that were based on the declining $FAPbI_3$ peak were very similar to the ones obtained from the growing PbI_2 peak, and since the PbI_2 is formed above the perovskite, the results based on the PbI_2 peak should not be affected at all by this phenomenon.

A recrystallization or reorientation of the material. There is the known transition from the δ phase to the α phase of $FAPbI_3$ at around 130 °C [38,39]. As can be seen in the colormap in Fig. 2 by the change in relative peak intensities, the $FAPbI_3$ film does respond to the increasing temperature by recrystallizing or changing the preferential orientation of the crystal grains. To limit the effect of this on the results of the isothermal decomposition experiments, an intermediate temperature at 160 °C was held for at least 20 min, before heating to the respective isothermal decomposition. It is also of note that the results for E and A that used the growing PbI_2 peak as their basis where similar to the values obtained from studying the declining $FAPbI_3$ peak. Since the growing PbI_2 peak should not be influenced by a recrystallization of the $FAPbI_3$ educt, this is a good indication that this phenomenon has no major impact on our results.

We would like to insert a short comment on an ongoing dispute concerning the interpretation of solid-state decomposition analysis. When using the Arrhenius approach to determine the reaction kinetics of a decomposition reaction from the solid state, it is of note, that the applicability of the Arrhenius equation to this class of reactions is, at this point, a contentious topic. This has to do with the fact that the base assumptions behind the Arrhenius model pertain to the theory of gases and liquids: The atoms, ions, or molecules in the reactant species move freely with a kinetic energy that is proportional to the temperature of the substance. If a collision with an energy of at least E occurs, it leads to a reaction. The frequency factor A describes how often these collisions happen and the term of the Maxwell-Boltzmann distribution [$\exp(-\frac{E}{RT})$, see Eq. (2)] gives the relative fraction of collisions that occur with an energy of at least E. Further restrictions as to which collisions lead to a reaction—such as requiring the collisions of specific bonds—are usually incorporated into the frequency factor [45]. According to Garn, the energies within solids are too equally spread out to allow for the application of Maxwell-Boltzmann statistics and thus there exists no distinct activated species [46]. This violates one of the central assumptions of the Arrhenius model and

immediately raises the question, what an empirically determined activation energy from a conventional Arrhenius plot actually signifies. A recent discussion of the current state of the theory of solid state decomposition is given in Ref. [47]. A promising contribution to this topic was made by L'vov, who developed the theory of congruent dissociative volatilization (CDV) that aims to close this explanatory gap. His theory is derived in detail in Refs.[48–50]. This theory retains the validity of the empiric relation described by Eq. (4), but here the activation energy E is assigned to the molar enthalpy $\Delta_r H_T^\circ/\nu$, thus relating the empirically determined value E to an actual physical property of the studied material. Just as important, it gives a theoretical foundation to the application of the Arrhenius relation. Additionally, it provides an explanation for the often observed "compensation effect", where similar experiments on the same substance lead to disparate results for A and E that, however, follow the relation $\ln A = aE + b$. The CDV theory proposes the following model reaction for solid-state decompositions:

$$R(s/l) \leftrightarrow S(g) + V(g) \rightarrow S(s) + V(g). \quad (9)$$

Here, a reactant R (liquid or gas) first reacts into two gaseous products, one of which volatile (V), that remains a gas, and one nonvolatile (S), that subsequently condenses to form a solid. When applied to the thermal decomposition of $FAPbI_3$ (ignoring any further decomposition of the FAI component) the equation is:

$$FAPbI_3(s) \leftrightarrow PbI_2(g) + FAI(g) \rightarrow PbI_2(s) + FAI(g). \quad (10)$$

Such a recondensation of PbI_2 would explain the very high crystallinity of the reaction product, as it was observed in our experiments. In our current paper, we are unable to add significant further insight into the applicability of the CDV theory. However, for completeness we mention it here in order to offer an alternative physical interpretation for the commonly extracted activation energies. Independent from the above discussion on their physical interpretation, the experimental data presented in this paper and the kinetic parameters extracted in the following sections allow to determine the temperature dependence of the degradation kinetics of $FAPbI_3$ in an empirical way, enabling the comparison with $MAPbI_3$ and the prediction of the degree of decomposition for a given set of time and temperature.

III. EXPERIMENTAL DETAILS

The sample preparation and posttreatment took place within a high vacuum chamber under a base pressure of 2×10^{-5} mbar. The $FAPbI_3$ thin films were deposited using thermal coevaporation of the precursors PbI_2 at 350 °C and FAI at 195 °C from Al_2O_3 crucibles. The pressure within the chamber increased to 7×10^{-5} mbar during the deposition of the films, mostly due to the evaporation of FAI. The target sample thickness was around 310 nm with an average growth rate of 0.13 Å s^{-1}. After the preparation, without interrupting the vacuum, the samples were heated via radiative heat from a carbon heating element at the back of the sample holder. During the whole process, including growth and annealing, the samples were observed using an *in situ* XRD system. The system had a fixed source-sample-detector geometry during the whole process and recorded one measurement every 60 s. The x-ray source was made of Cu and a Ni filter was used to reduce the strength of the Cu k_β reflexes. The detector was composed of three Dectris Mythen 1 K modules, that together cover a 2θ range of 28°. More information about the preparation and analysis apparatus can be found in Ref. [13].

In line with previous experiments, we first exposed a freshly deposited $FAPbI_3$ layer to a temperature ramp of 3.6 K min^{-1}, starting at room temperature, to investigate the phase evolution and to determine the onset of decomposition.

For the isothermal experiments, the samples were heated to either 230 °C, 250 °C, 270 °C, or 290 °C. In order to ensure that the initial $FAPbI_3$ thin film was completely in the photoactive α phase and in order to avoid recrystallization effects observed at lower temperatures, an intermediate temperature step at 160 °C for at least 20 min was introduced prior to applying the actual isothermal decomposition temperature.

For the preparation of the partially decomposed sample, half of the sample was covered by a stainless steel plate, partially shielding the sample from the heater. This cover was applied after the $FAPbI_3$ deposition, in a nitrogen filled glovebox attached to the deposition chamber, therefore ensuring that the sample would not come into contact with ambient air. The decomposition process kept the sample at 250 °C for 50 min. Due to the shield, the sample was effectively exposed to a temperature gradient over its length.

IV. RESULTS

A. Growth

To grow the perovskite, FAI and PbI_2 have been thermally coevaporated in a high vacuum chamber. More details on the growth conditions can be found in Sec. III. A colormap representation of the growth process is shown in Fig. 1. The XRD peaks that became detectable upon the formation of the perovskite correspond well to either the black α phase or the yellow δ phase of $FAPbI_3$. The peaks of the α phase have been indexed using the PDF reference 00-069-0999 and the δ-phase peaks have been indexed according to Han *et al.*'s work in Ref. [38]. The visible peaks of the α phase are: (100) [13.92°], (110) [19.70°], (111) [24.51°], (200) [28.00°], (210) [31.39°]. From the δ phase, the following peaks are detected: (002) [22.39°], (021) [25.36°], ($\bar{1}$22) [30.52°], (004) [32.80°]. Additionally, the ($\bar{1}$30) peak of the δ phase might exist, but is overlayed by the (210) peak of the α phase. The δ phase vanished after heating the samples to 160 °C for twenty minutes and only the α phase remained.

B. Temperature ramp experiment

To identify any phase changes that might occur during annealing, a freshly prepared film was subjected to a temperature ramp. Below 160 °C, for the peaks assigned to the α-$FAPbI_3$ phase, no decomposition but only a recrystallization was observed, which manifested in variations of the relative peak intensities. For temperatures above 230 °C, the intensities of the perovskite peaks rapidly decreased until disappearing above approximately 270 °C, as can be observed in Fig. 2. In parallel to the decomposition of $FAPbI_3$, PbI_2 is formed. For temperatures above 290 °C, the PbI_2 decomposes and

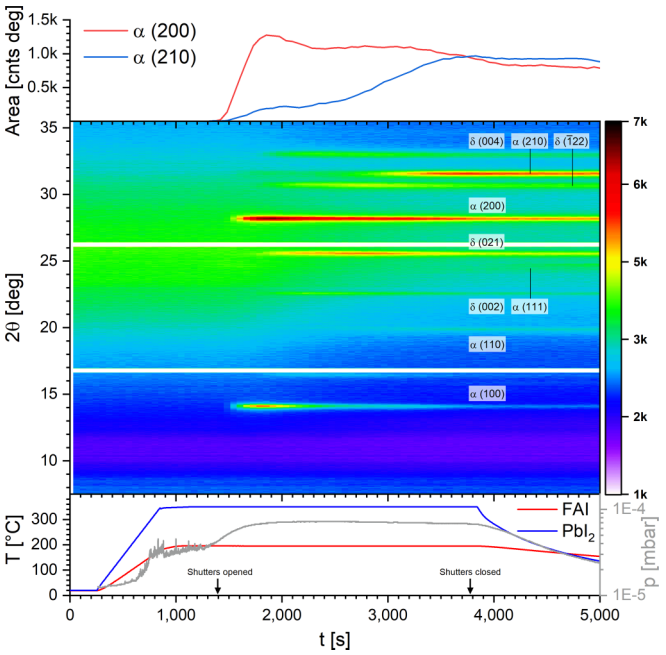

FIG. 1. Colormap of the growth of the $FAPbI_3$ perovskite that was used in the isothermal decomposition experiment at 290 °C. Every column of pixels corresponds to one XRD scan and the color indicates the number of counts received at the respective angle. The bottom graph shows the temperatures of the crucibles, the opening and closing times of the shutters and the chamber pressure. The XRD peaks are labeled by phase and miller index.

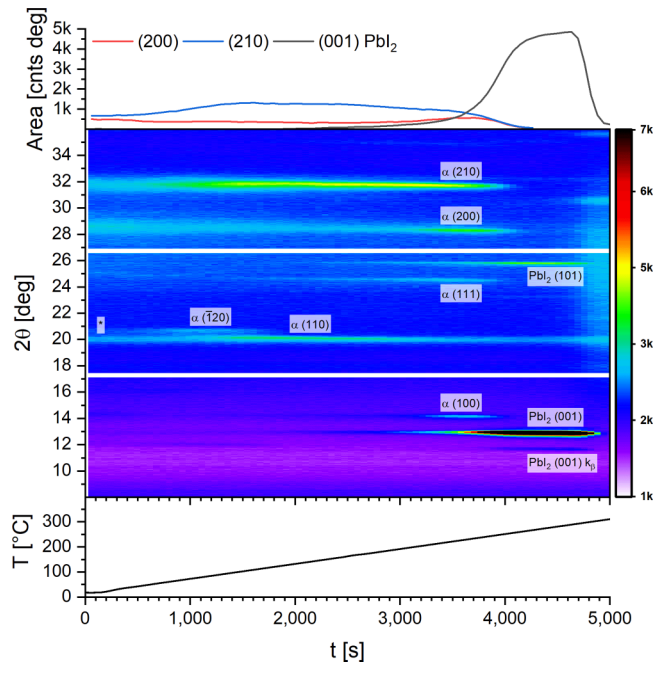

FIG. 2. Colormap of the temperature ramp experiment of the thermal decomposition of $FAPbI_3$. The top graph shows the integrated intensity of the (200) and (210) peaks of the α phase and the bottom graph shows the sample's temperature. An additional peak detected at 20° for this deposition run was identified with contamination of the Kapton window and is labeled with an asterisk in the graph. Notably, the (110) peak of the α phase overlays this peak for a time before the perovskite fully disappears.

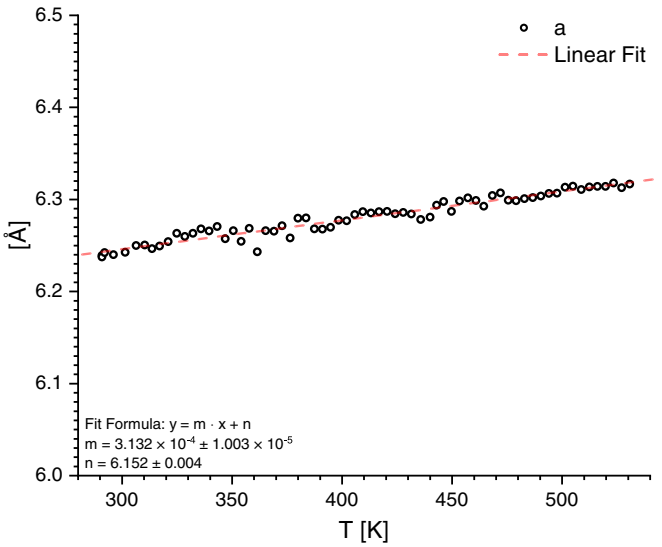

FIG. 3. Dependence of the lattice constant a on the temperature T together with a linear fit over the data. a has been calculated using the position of the (200) $FAPbI_3$ peak.

some metallic lead is detected. It is of note that with this experimental setup we cannot detect organic (and possibly volatile) decomposition products and as such we cannot make a comment as to whether the decomposition is driven by the dissociation of the FA molecule itself, as is the case for $MAPbI_3$, or whether the FA molecule stays intact during the decomposition. However, in works by Juarez-Perez et al. the FA decomposition products HCN and NH_3 have been detected during the thermal decomposition of $FAPbI_3$ and $FAPbBr_3$ [33].

Since the positions of the XRD peaks directly depend on the lattice constant of the analyzed material, their shift upon heating with a temperature ramp allows for the calculation of the thermal expansion coefficient of a material. Figure 3 shows the change of the lattice constant in relation to the temperature together with a linear fit of the data, as calculated from the (200) peak. α_L was also calculated from the positions of the (100), (110), (111), and (210) $FAPbI_3$ peaks in the XRD pattern for each scan. Since most of these other peaks were only faintly visible or not very sharp, a weighted average was taken and the result was $\alpha_L = 48.08 \pm 1.32 \times 10^{-6}\,\mathrm{K}^{-1}$. The results for the separate peaks can be found in the Supplemental Material [42]. Due to the deviations in the results for the different peaks, we would estimate the actual relative uncertainty of the end result to be closer to 10 %, resulting in a final value of $\alpha_L = 48 \pm 5 \times 10^{-6}\,\mathrm{K}^{-1}$. This value for the linear thermal expansion coefficient for $FAPbI_3$ is higher than the value we obtained, using the same method, for $MAPbI_3$ thin films in Ref. [13], which is $36 \pm 1 \times 10^{-6}\,\mathrm{K}^{-1}$.

C. Partial decomposition - SEM/EDX analysis

As described in Sec. III, one sample was partially decomposed by applying a temperature gradient over its surface. One sample was taken out of the vacuum chamber prior to annealing, serving as an untreated reference sample. The sample turned orange upon exposure to ambient air, which indicates

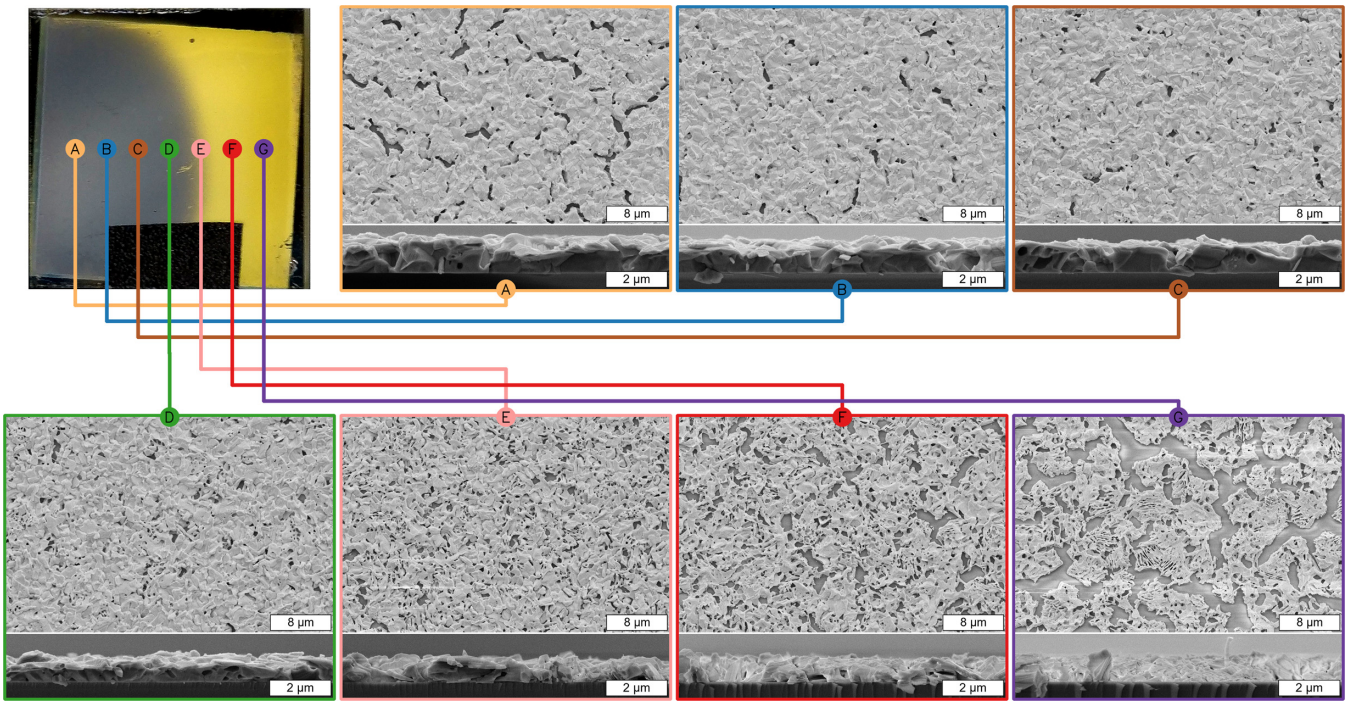

FIG. 4. Cross-sectional and top view SEM images of the partially decomposed sample. The photograph at the top left marks the approximate areas where the SEM images were taken. The cross section images correspond approximately to the positions of the surface images.

the transition from the α to the δ phase. This untreated sample was analyzed with a scanning electron microscope (SEM) in this state. The resulting images are shown in Figs. 5(a) and 5(b). The images were taken by two detectors (consecutively, not simultaneously): an Everhart-Thornley secondary electron detector (ET-SE) and an in-lens secondary electron detector (IL-SE). The ET-SE image (a), shows a smooth layer with full coverage and particles of roughly 300 nm in average size. The IL-SE image (b), which provides a higher material contrast, suggests a very homogeneous layer without any visible secondary phases.

The succession of SEM images shown in Fig. 4 provides an insight into the progress of the reaction and the resulting morphology change on a microscopic scale. Going from left to right (lower to higher annealing temperature), the sample first shows only very small signs of decomposition while the decomposition gets more pronounced towards the right side. Image *A* is an exception to this, because the metal rail that blocked the thermal radiation let some heat through on the leftmost side. Because of this, the part of the sample which is least decomposed is shown in images *B* and *C*. Some rifts are already visible at these positions, while the layer still covers most of the sample. At point *D*, roughly in the middle of the sample, some pores and voids appear. The cross section shows a declining layer thickness and hints at flat platelets forming at the top of the layer. Their characteristic form suggests a hexagonal crystal structure, as expected for the decomposition product PbI_2, that was detected with XRD. Figures 5(c) and 5(d) show the same spot of the image with a larger magnification and, in addition to the ET-SE image, also shows an IL-SE image. Due to the higher material contrast of the IL-SE image, two clearly distinct phases are visible. The brighter part of the image with the hexagonal platelet structures is assigned to PbI_2, as indicated above. The slightly darkened spot in the middle is likely an artifact of the IL-SE system, as those detectors can sometimes lead to a small dark area at the center of the image. Overall, this image gives the impression that $FAPbI_3$ (in dark) is overlayed by the brighter PbI_2, consistent with the cross-section image of *D* in Fig. 4, indicating the formation of a PbI_2 top layer. The next image (*E*) shows an increase in porousness and the PbI_2 platelets are now clearly visible in the cross section. This is also the part of the sample where, in the photo, the dark perovskite area gives way to the yellow PbI_2. In image *F*, which in the photo is already completely yellow, the layer coverage has decreased significantly. The pores from before have now started forming elongated ridges. On position *G*, the sample exhibits a very low surface coverage and what remains of the layer is highly furrowed. The cross section underlines this by showing a layer that has significantly lost in thickness and looks more like a loose scattering of material, rather than a solid layer. EDX measurements of the [I]/[Pb] ratio (IP) taken on positions *A*, *D,* and *G*, which are shown in Table I, are consistent with these visual observations. Positions *A*'s and *D*'s IPs are close to the value expected for $FAPbI_3$ (IP $\approx$ 3), while the results for position *G* indicate that PbI_2 has been formed (IP $\approx$ 2), which is consistent with the expectations.

D. Isothermal decomposition - First order approach

To calculate the kinetic parameters of the thermal decomposition reaction, a set of isothermal decomposition

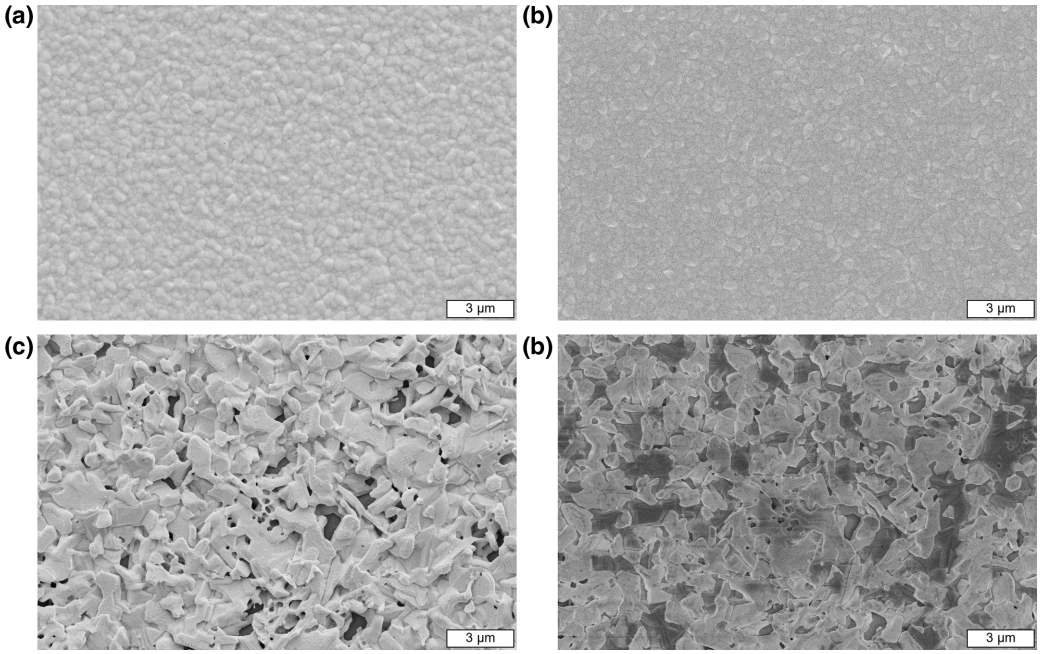

FIG. 5. (a) Everhart-Thornley secondary electron (ET-SE) micrograph of an untreated sample. (b) Micrograph using the in-lens secondary electron detector (IL-SE) of the same area of an untreated sample. (c) ET-SE image of the partially decomposed sample at position *D* (see Fig. 4). (d) IL-SE image of the same area of the partially decomposed sample.

experiments has been conducted at temperatures of 230 °C, 250 °C, 270 °C, and 290 °C. In the first experiment at 230 °C, the area of the perovskite peaks declined by only 50 % over 3.5 h. An overview of the results is depicted in Fig. 6. The sample annealed at 250 °C showed recrystallization prior to decomposition: After the final temperature of 250 °C was reached, the (111) and (200) peaks gained notably in intensity over several minutes before declining. The (210) peak did not exhibit this behavior. After the initial increase, the following decline of the (111) and (200) peaks was far more rapid than that of the (210) peak. In consequence, the initial recrystallization might lead to an overestimation of the subsequent intensity decay and reaction rate k, when considering merely the (111) and (200) peaks. For these reasons, the evaluation is focused on the decline of the $FAPbI_3$ (210) peak. Since the decomposition of $FAPbI_3$ results in a crystalline PbI_2 layer, the formation of this reaction product also constitutes an indicator for the progress of the decomposition reaction and is decoupled from any recrystallization effects occurring in the $FAPbI_3$ layer. Therefore, the rise of the PbI_2 (001) peak is used as a second variable for the calculation of the reaction rate k. For better comparability with the declining peak areas of the $FAPbI_3$ reflexes, the normalized peak areas a of the PbI_2 reflexes are given as $(1 - a)$ in Fig. 7.

In order to determine a first estimate for the the reaction rate k, the data points were fitted using the exponential equation of Eq. (3). Since the exact beginning of the decomposition can be difficult to determine, the first 4 to 5 data points were ignored and the fit was conducted down to a normalized peak

TABLE I. EDX measurements of different positions in Fig. 4. The values are given as the amount of I atoms per one Pb atom, which is the [I]/[Pb] ratio, also referred to here as IP. For $FAPbI_3$ the expected IP is 3 and for PbI_2 it is 2.

Position	I per Pb (IP)
A	3.2
D	2.9
G	2.1

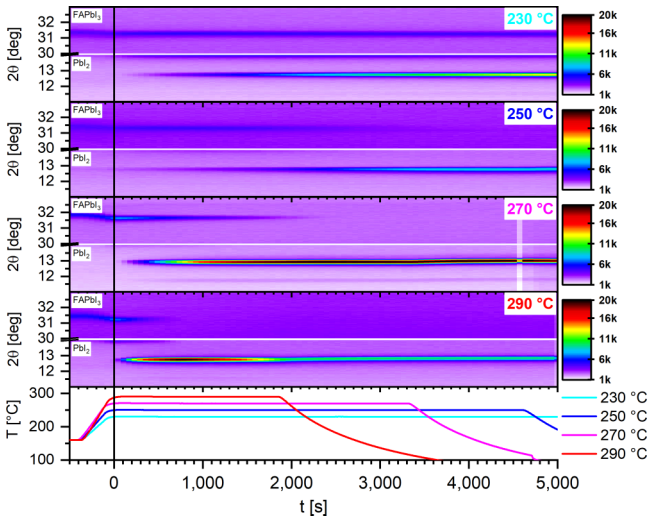

FIG. 6. Colormaps of the decomposition experiments. The decay of the (210) $FAPbI_3$ peak is visible in the 30° to 33° range and the growth of the (001) PbI_2 peak is visible in the 11° to 14° range. The substrate temperatures for each of these experiments are shown in the bottom graph.

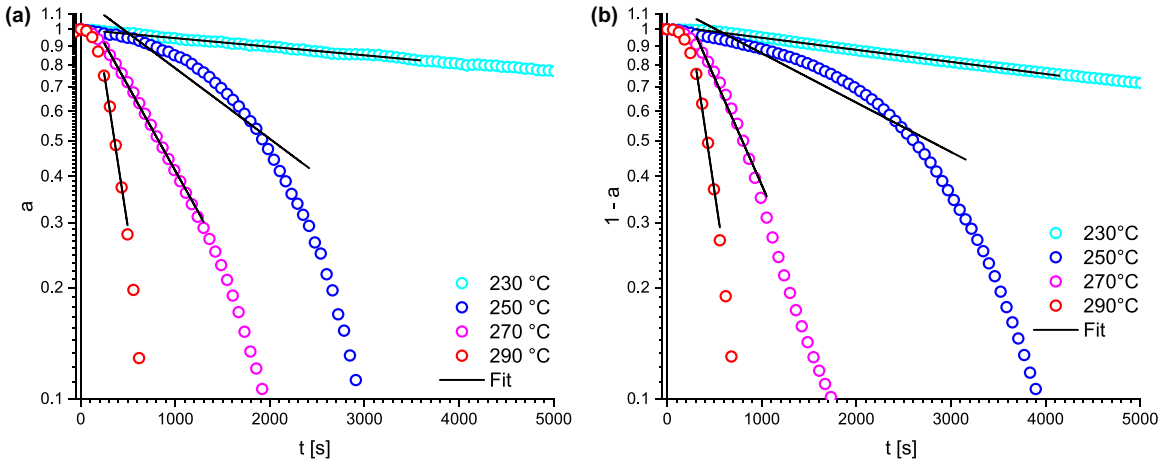

FIG. 7. Logarithmic plots of the time evolution of the normalized peak areas a together with the linear fits. (a) Normalized peak area a for the (210) peak of $FAPbI_3$. (b) The evolution of the (001) PbI_2 peak. In this latter case, one minus the normalized peak area $(1 - a)$ is plotted for better comparability.

area a of 0.3. This is possible because for a first-order decay, the speed of the reaction does not depend on the extent of the reaction. The 250 °C process does not fit this exponential decay as well as the others, but the fit range was chosen by the same criteria for consistency. The process using 230 °C is the only exception to this, since the area of the perovskite peaks only dropped to 50 % during the course of the experiment. However, since it showed a very consistent exponential decay, the result is quite insensitive to the choice of the fit range. After obtaining a value for k for each experiment, $\ln k$ has been plotted over $1/T$ to achieve an Arrhenius-type plot, which is depicted in Fig. 8 for the (210) peak of $FAPbI_3$ and the (001) peak of PbI_2, together with the plot resulting from averaging over the k values for the (210) $FAPbI_3$ peak and the (001) PbI_2 peak. The exponential fits shown in Fig. 7 provide a statistical error σ for each value of k and these errors have been used in the Arrhenius fits to weight the data according to $w_i = 1/\sigma_i$. The resulting fit for the averaged values of k yielded values for the activation energy $E = 165.3 \pm 4.9\,\mathrm{kJ\ mol^{-1}}$ and the pre-exponential factor $\ln A = 29.9 \pm 1.2$. The results of these evaluations are summarized in Table II.

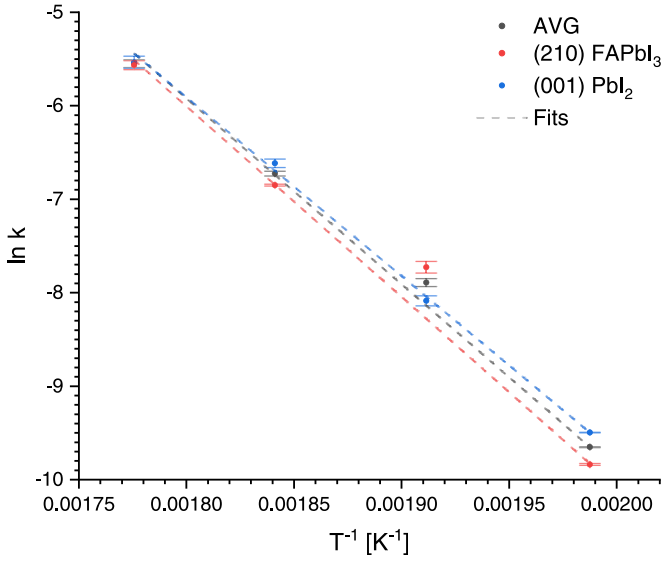

FIG. 8. Arrhenius plot showing $\ln k$ values over $1/T$ for the (210) peak of $FAPbI_3$ and the (001) peak of PbI_2. "AVG" denotes the averaged k values. The values for k are determined from the exponential fits of the graphs shown in Fig. 7. The errors of $\ln k$, as calculated from the statistical errors of the exponential fits, are marked with horizontal lines. For the linear fits, the data points were weighted with these errors σ according to $w_i = 1/\sigma_i$.

E. Model-fitting approach

Our paper on $MAPbI_3$ (Ref. [10]) showed the difficulty to determine a specific reaction model from our data. In addition, the obtained E and A values did not significantly deviate from the ones obtained from the manual first order fitting method. We made a similar comparison with the same set of reaction models for the data on $FAPbI_3$ obtained here. The outcome was similar to the $MAPbI_3$ case, as the linearity of the $g(\alpha)$ over t plot (a rough measure for how well a model fits the reaction) and the values for E and A were similar for many of the models. The specific results for all models are included in the supporting information [42]. The evaluation of the (210) $FAPbI_3$ peak with the different reaction models resulted in values of $E \approx 150 \pm 24\,\mathrm{kJ\ mol^{-1}}$ and $\ln A = 26 \pm 5$, while the (001) PbI_2 peak yielded $E \approx 160 \pm 16\,\mathrm{kJ\ mol^{-1}}$ and $\ln A = 28 \pm 4$.

TABLE II. Results of the first order approach for the (210) $FAPbI_3$ peak and the (001) PbI_2 peak. The result that was obtained by averaging the k values of these two peaks for each temperature is denoted as "AVG".

Peak	E [kJ mol^{-1}]	$\ln A$ [s^{-1}]
(210) $FAPbI_3$	169.1 ± 3.6	30.6 ± 0.9
(001) PbI_2	159.1 ± 2.9	28.5 ± 0.7
AVG	165.3 ± 4.9	29.9 ± 1.2

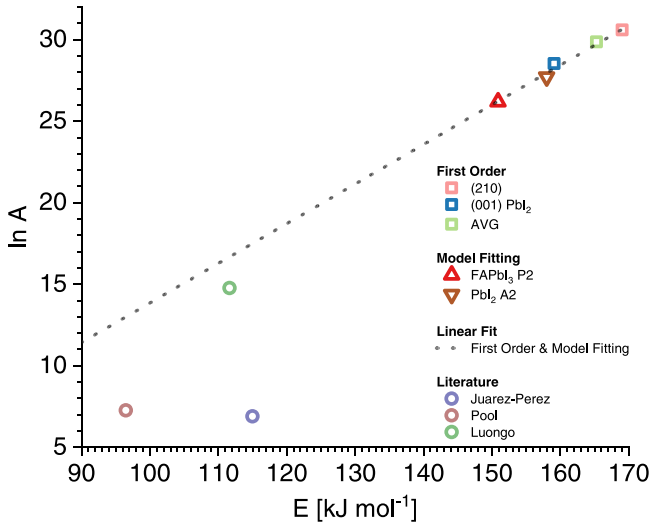

FIG. 9. The results of this paper depicted as an $\ln A$ over E plot, together with the results of Juarez-Perez *et al.* [33], Pool *et al.* [34], and Luongo *et al.* [35]. The linear fit is indicated by the dotted line.

F. Compensation effect

Just as in our previous paper, we again found that the results of the various methods and reaction models follow a line with the form

$$\ln A = a\,E + b. \tag{11}$$

The $\ln A$ over E data is plotted in Fig. 9. This behavior is generally known as the compensation effect, which refers to the phenomenon that similar experiments on the decomposition of a material can lead to a significant spread of E and $\ln A$ values, while those values are coupled by a linear dependence. The line described by Eq. (11) implies that there is a temperature T at which these processes agree on a specific turnover ratio k. From the values of a and b one can calculate these values for T and k:

$$T = \frac{1}{R\,a} \tag{12}$$

$$\ln k = b. \tag{13}$$

A linear fit of the data presented in Fig. 9 gave values of $a = 0.243 \pm 0.022$ and $b = -10.453 \pm 3.553$, which results in a temperature of agreement of $T = 222 \pm 45\,^{\circ}\mathrm{C}$ and a corresponding turnover ratio of $\ln k = 10.453 \pm 3.553$. L'vov's theory of CDV explains the compensation effect with the buildup of product gases in the reactor, that influence the values for E and A according to Eq. (11). Unfortunately, since all our experiments were conducted in high vacuum, this explanation does not apply to our case. A more likely explanation is the simple fact that, because the evaluations used the same experimental data, their results need to agree on the overall turnover ratio to some degree, but the specific values for E and A are more sensitive to small deviations in the data and the choice of the evaluation method.

When comparing the results of our paper with the other works mentioned in Table III, the results of Luongo *et al.* are close to the linear fit line shown in Fig. 9, hinting at an overall similar rate of decomposition.

V. DISCUSSION

The activation energy of the thermal decomposition of $FAPbI_3$ that has been determined in this paper ($E = 165\,\mathrm{kJ\,mol^{-1}}$) is significantly larger than that which has been determined for $MAPbI_3$ ($E = 110\,\mathrm{kJ\,mol^{-1}}$) in our previous paper [10]. However, it needs to be stressed that this does not by itself indicate a higher thermal stability, i.e., a lower rate of thermal decomposition at any given temperature. To make such an assessment, the rate constant A needs to be taken into account as well. According to Eq. (2), the activation energy E determines how k changes with a change in temperature T, while the rate constant A is a scalar factor onto the exponential term that, especially in the field of solid-state decompositions, can vary by many orders of magnitude between different processes [51]. To get an understanding of how the values for E and A, taken together, translate into the thermal stability of a material, one can use Eq. (2) to calculate $k(T)$. Figure 10 shows the calculated $k(T)$ relation for $FAPbI_3$ and $MAPbI_3$ (with E and A taken from Ref. [10]), together with the experimentally determined values for k. The figure also shows the temperature difference between $k(T)$ of $MAPbI_3$ and $k(T)$ of $FAPbI_3$ for a given rate k. From this it can be estimated that the start of the decomposition of $FAPbI_3$ is shifted upwards by about 45 °C when compared to $MAPbI_3$, while the temperature difference between the two curves becomes smaller as the temperature increases.

Overall, the results confirm the higher thermal stability of $FAPbI_3$ when compared to $MAPbI_3$. While Fig. 10 implies an upwards shift of the temperature of thermal decomposition by only roughly 45 °C, the increased stability becomes more apparent when looking at the predicted decomposition

TABLE III. Comparison of the results and experimental methods of this work with the works of Juarez-Perez *et al.* [33], Pool *et al.* [34], and Luongo *et al.* [35]. The results of Luongo *et al.* are divided into three parts. A: *In situ* XRD of the whole decomposition process; B: Differential scanning calorimetry (DSC) of the first decomposition step; C: DSC of the second decomposition step.

Source	E [kJ mol^{-1}]	$\ln A$ [s^{-1}]	Configuration	Preparation	Atmosphere	T-regime	Measured value
This paper	165.3 ± 4.9	29.9 ± 1.2	Thin film	Coevaporation	Vacuum	Isothermal	Time-resolved XRD
[33]	115 ± 3	6.9 ± 0.2	Powder	Solution + Mortar	Vacuum & He	Ramp	TGA
[34]	96.5 ± 13.1	7.260 ± 0.007	Thin Film	Spin-coating	N_2	Ramp	Time-resolved XRD
[35] A	112 ± 9	14.8 ± 2.0	Powder	Grinding of precursors	He	Ramp	Time-resolved XRD
[35] B	205 ± 20	–	Powder	Grinding of precursors	Ar	Ramp	DSC
[35] C	410 ± 20	–	Powder	Grinding of precursors	Ar	Ramp	DSC

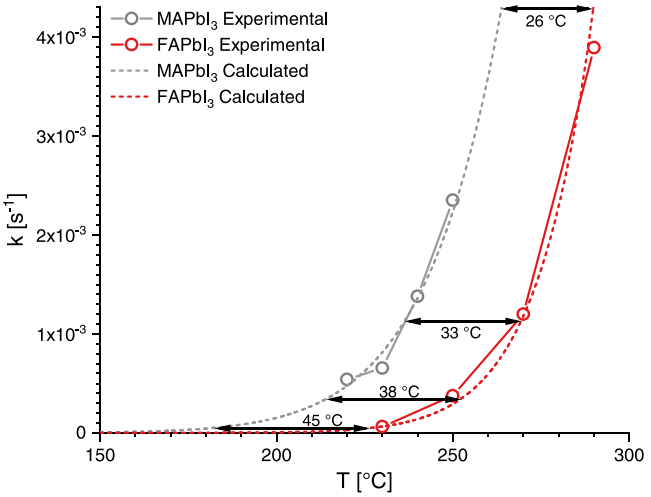

FIG. 10. Comparison of how the rate constant of the thermal decomposition k depends on the temperature T for $MAPbI_3$ (data taken from our earlier work in Ref. [10]) and $FAPbI_3$ (data taken from this paper). The circles represent the k values obtained from the measurements and the dotted lines are calculations using Eq. (2), with $E = 110.5\,\mathrm{kJ\,mol^{-1}}$ and $\ln A = 19.3$ for $MAPbI_3$ and $E = 165.3\,\mathrm{kJ\,mol^{-1}}$ and $\ln A = 29.9$ in the case of $FAPbI_3$. The arrows show the difference in temperature between the two calculated curves for the same value of k.

behavior at lower temperatures. In our paper on $MAPbI_3$ [10] we calculated the time in which the perovskite would decompose by 20 % to $\alpha = 0.2$ at 85 °C and the result was 2800 h (around 120 d). For $FAPbI_3$ to decompose to the same extent at 85 °C, it would take roughly 8 000 000 h (around 900 years). A similar calculation stated that for $MAPbI_3$ to not decompose by more than 20 % within 1 h it would need to be stored below 180 °C. In the case of $FAPbI_3$ this temperature would be 230 °C. Zhang *et al.* note that, compared to MA, FA is a larger molecule with a smaller dipole moment and, in perovskites, has a larger bonding strength to the halides, which reduces halide ion migration and explains the higher stability commonly observed with FA-based perovskites [52,53].

VI. CONCLUSIONS

In conclusion, we have determined the kinetic parameters for the thermal decomposition of coevaporated $FAPbI_3$ thin films, deriving an activation energy of $E = 165.3 \pm 4.9\,\mathrm{kJ\,mol^{-1}}$ and a pre-exponential factor of $\ln A = 29.9 \pm 1.2$. The data indicates that the onset of decomposition occurs at higher temperatures compared to $MAPbI_3$, which confirms the higher thermal stability of the FA-based perovskite. The temperature ramp experiment indicated the start of the decomposition of $FAPbI_3$ to occur at roughly 230 °C, which is in good agreement with what would be expected from the determined values for E and A. The linear expansion coefficient was determined to be $\alpha_L = 48 \pm 5 \times 10^{-6}\,\mathrm{K^{-1}}$. The SEM analysis of the partially decomposed sample indicated a decomposition that started from the top of the layer, forming PbI_2, and progressed through the whole layer while significantly reducing its surface coverage.

ACKNOWLEDGMENTS

We gratefully acknowledge financial support from the German Federal Ministry of Research and Education (BMBF) under Contract No. 03EK3570B (StrukturSolar II) and from the Spanish Ministerio de Universidades under the Beatriz Galindo Senior Program No. BG20/00194.

There are no conflicts of interest to disclose.

[1] A. Kojima, K. Teshima, Y. Shirai, and T. Miyasaka, Organometal halide perovskites as visible-light sensitizers for photovoltaic cells, J. Am. Chem. Soc. **131**, 6050 (2009).

[2] Y. C. Kim, K. H. Kim, D.-Y. Son, D.-N. Jeong, J.-Y. Seo, Y. S. Choi, I. T. Han, S. Y. Lee, and N.-G. Park, Printable organometallic perovskite enables large-area, low-dose x-ray imaging, Nature (London) **550**, 87 (2017).

[3] H. Wei and J. Huang, Halide lead perovskites for ionizing radiation detection, Nat. Commun. **10**, 1066 (2019).

[4] Q. Shan, J. Song, Y. Zou, J. Li, L. Xu, J. Xue, Y. Dong, B. Han, J. Chen, and H. Zeng, High performance metal halide perovskite light-emitting diode: From material design to device optimization, Small **13**, 1701770 (2017).

[5] Y. Sun, L. Zhang, N. Wang, S. Zhang, Y. Cao, Y. Miao, M. Xu, H. Zhang, H. Li, C. Yi, J. Wang, and W. Huang, The formation of perovskite multiple quantum well structures for high performance light-emitting diodes, npj Flex. Electron. **2**, 12 (2018).

[6] M. Yuan, L. N. Quan, R. Comin, G. Walters, R. Sabatini, O. Voznyy, S. Hoogland, Y. Zhao, E. M. Beauregard, P. Kanjanaboos, Z. Lu, D. H. Kim, and E. H. Sargent, Perovskite energy funnels for efficient light-emitting diodes, Nat. Nanotechnol. **11**, 872 (2016).

[7] N. Wang, L. Cheng, R. Ge, S. Zhang, Y. Miao, W. Zou, C. Yi, Y. Sun, Y. Cao, R. Yang *et al.*, Perovskite light-emitting diodes based on solution-processed self-organized multiple quantum wells, Nat. Photonics **10**, 699 (2016).

[8] S. W. Eaton, M. Lai, N. A. Gibson, A. B. Wong, L. Dou, J. Ma, L.-W. Wang, S. R. Leone, and P. Yang, Lasing in robust cesium lead halide perovskite nanowires, Proc. Natl. Acad. Sci. USA **113**, 1993 (2016).

[9] C. C. Boyd, R. Cheacharoen, T. Leijtens, and M. D. McGehee, Understanding degradation mechanisms and improving stability of perovskite photovoltaics, Chem. Rev. **119**, 3418 (2019).

[10] T. Burwig and P. Pistor, Reaction kinetics of the thermal decomposition of $MAPbI_3$ thin films, Phys. Rev. Materials **5**, 065405 (2021).

[11] P. Holzhey and M. Saliba, A full overview of international standards assessing the long-term stability of perovskite solar cells, J. Mater. Chem. A **6**, 21794 (2018).

[12] S. Zhang and G. Han, Intrinsic and environmental stability issues of perovskite photovoltaics, Prog. Energy **2**, 022002 (2020).

[13] P. Pistor, T. Burwig, C. Brzuska, B. Weber, and W. Fränzel, Thermal stability and miscibility of co-evaporated methyl ammonium lead halide ($MAPbX_3$, X = I, Br, Cl) thin films analysed by *in situ* x-ray diffraction, J. Mater. Chem. A**6**, 11496 (2018).

[14] A. Dualeh, P. Gao, S. I. Seok, M. K. Nazeeruddin, and M. Grätzel, Thermal behavior of methylammonium lead-trihalide perovskite photovoltaic light harvesters, Chem. Mater. **26**, 6160 (2014).

[15] N.-K. Kim, Y. H. Min, S. Noh, E. Cho, G. Jeong, M. Joo, S.-W. Ahn, J. S. Lee, S. Kim, K. Ihm, *et al.*, Investigation of thermally induced degradation in $CH_3NH_3PbI_3$ perovskite solar cells using *in-situ* synchrotron radiation analysis, Sci. Rep. **7**, 4645 (2017).

[16] E. J. Juarez-Perez, Comment on probing the origins of photodegradation in organic- inorganic metal halide perovskites with time-resolved mass spectrometry, sustainable energy & fuels, ChemRxiv (2018), doi: 10.26434/chemrxiv.7295585.v2.

[17] H. A. Dewi, J. Li, H. Wang, B. Chaudhary, N. Mathews, S. Mhaisalkar, and A. Bruno, Excellent intrinsic long-term thermal stability of co-evaporated $MAPbI_3$ solar cells at 85 °C, Adv. Funct. Mater. **31**, 2100557 (2021).

[18] T. Burwig, W. Fränzel, and P. Pistor, Crystal phases and thermal stability of co-evaporated $CsPbX_3$ (X = I, Br) thin films, J. Phys. Chem. Lett. **9**, 4808 (2018).

[19] T. Burwig, K. Heinze, V. Naumann, A. Hähnel, S. Lange, C. Hagendorf, R. Scheer, and P. Pistor, Co-evaporated $Cs_2AgBiBr_6$ double perovskites for solar cells, in *Proceedings of the 36th European Photovoltaic Solar Energy Conference and Exhibition* (WIP, Marseille, France, 2019) pp. 728–732.

[20] T. Burwig, M. Guc, V. Izquierdo-Roca, and P. Pistor, Synthesis and crystal structure evolution of co-evaporated $Cs_2AgBiBr_6$ thin films upon thermal treatment, J. Phys. Chem. C **124**, 9249 (2020).

[21] G. Niu, W. Li, J. Li, X. Liang, and L. Wang, Enhancement of thermal stability for perovskite solar cells through cesium doping, RSC Adv. **7**, 17473 (2017).

[22] X. Li, J. Wu, S. Wang, and Y. Qi, Progress of all-inorganic cesium lead-free perovskite solar cells, Chem. Lett. **48**, 989 (2019).

[23] G. A. Tosado, Y.-Y. Lin, E. Zheng, and Q. Yu, Impact of cesium in phase and device stability of triple cation Pb-Sn double halide perovskite films and solar cells, J. Mater. Chem. A **6**, 17426 (2018).

[24] R. E. Beal, D. J. Slotcavage, T. Leijtens, A. R. Bowring, R. A. Belisle, W. H. Nguyen, G. F. Burkhard, E. T. Hoke, and M. D. McGehee, Cesium lead halide perovskites with improved stability for tandem solar cells, J. Phys. Chem. Lett. **7**, 746 (2016).

[25] B. wook Park and S. I. Seok, Intrinsic instability of inorganic–organic hybrid halide perovskite materials, Adv. Mater. **31**, 1805337 (2019).

[26] E. Smecca, Y. Numata, I. Deretzis, G. Pellegrino, S. Boninelli, T. Miyasaka, A. L. Magna, and A. Alberti, Stability of solution-processed $MAPbI_3$ and $FAPbI_3$ layers, Phys. Chem. Chem. Phys. **18**, 13413 (2016).

[27] A. F. Akbulatov, S. A. Tsarev, M. Elshobaki, S. Y. Luchkin, I. S. Zhidkov, E. Z. Kurmaev, S. M. Aldoshin, K. J. Stevenson, and P. A. Troshin, Comparative intrinsic thermal and photochemical stability of Sn(II) complex halides as next-generation materials for lead-free perovskite solar cells, J. Phys. Chem. C **123**, 26862 (2019).

[28] M. Saliba, T. Matsui, J.-Y. Seo, K. Domanski, J.-P. Correa-Baena, M. K. Nazeeruddin, S. M. Zakeeruddin, W. Tress, A. Abate, A. Hagfeldt, and M. Grätzel, Cesium-containing triple cation perovskite solar cells: Improved stability, reproducibility and high efficiency, Energy Environ. Sci. **9**, 1989 (2016).

[29] A. F. Akbulatov, S. Y. Luchkin, L. A. Frolova, N. N. Dremova, K. L. Gerasimov, I. S. Zhidkov, D. V. Anokhin, E. Z. Kurmaev, K. J. Stevenson, and P. A. Troshin, Probing the intrinsic thermal and photochemical stability of hybrid and inorganic lead halide perovskites, J. Phys. Chem. Lett. **8**, 1211 (2017).

[30] A. F. Akbulatov, V. M. Martynenko, L. A. Frolova, N. N. Dremova, I. Zhidkov, S. A. Tsarev, S. Y. Luchkin, E. Z. Kurmaev, S. M. Aldoshin, K. J. Stevenson, and P. A. Troshin, Intrinsic thermal decomposition pathways of lead halide perovskites $APbX_3$, Sol. Energy Mater. Sol. Cells **213**, 110559 (2020).

[31] G. E. Eperon, S. D. Stranks, C. Menelaou, M. B. Johnston, L. M. Herz, and H. J. Snaith, Formamidinium lead trihalide: A broadly tunable perovskite for efficient planar heterojunction solar cells, Energy Environ. Sci. **7**, 982 (2014).

[32] J.-W. Lee, D.-J. Seol, A.-N. Cho, and N.-G. Park, High-efficiency perovskite solar cells based on the black polymorph of $HC(NH_2)_2PbI_3$, Adv. Mater. **26**, 4991 (2014).

[33] E. J. Juarez-Perez, L. K. Ono, and Y. Qi, Thermal degradation of formamidinium based lead halide perovskites into sym-triazine and hydrogen cyanide observed by coupled thermogravimetry-mass spectrometry analysis, J. Mater. Chem. A **7**, 16912 (2019).

[34] V. L. Pool, B. Dou, D. G. V. Campen, T. R. Klein-Stockert, F. S. Barnes, S. E. Shaheen, M. I. Ahmad, M. F. A. M. van Hest, and M. F. Toney, Thermal engineering of $FAPbI_3$ perovskite material via radiative thermal annealing and *in situ* XRD, Nat. Commun. **8**, 14075 (2017).

[35] A. Luongo, B. Brunetti, S. V. Ciprioti, A. Ciccioli, and A. Latini, Thermodynamic and kinetic aspects of formamidinium lead iodide thermal decomposition, J. Phys. Chem. C **125**, 21851 (2021).

[36] M. T. Weller, O. J. Weber, J. M. Frost, and A. Walsh, Cubic perovskite structure of black formamidinium lead iodide, α-$[HC(NH_2)_2]PbI_3$, at 298 k, J. Phys. Chem. Lett. **6**, 3209 (2015).

[37] C. C. Stoumpos, C. D. Malliakas, and M. G. Kanatzidis, Semiconducting tin and lead iodide perovskites with organic cations: Phase transitions, high mobilities, and near-infrared photoluminescent properties, Inorg. Chem. **52**, 9019 (2013).

[38] Q. Han, S.-H. Bae, P. Sun, Y.-T. Hsieh, Y. M. Yang, Y. S. Rim, H. Zhao, Q. Chen, W. Shi, G. Li, and Y. Yang, Single crystal formamidinium lead iodide ($FAPbI_3$): Insight into the structural, optical, and electrical properties, Adv. Mater. **28**, 2253 (2016).

[39] A. Binek, F. C. Hanusch, P. Docampo, and T. Bein, Stabilization of the trigonal high-temperature phase of formamidinium lead iodide, J. Phys. Chem. Lett. **6**, 1249 (2015).

[40] X. Zheng, C. Wu, S. K. Jha, Z. Li, K. Zhu, and S. Priya, Improved phase stability of formamidinium lead triiodide perovskite by strain relaxation, ACS Energy Lett. **1**, 1014 (2016).

[41] S. Vyazovkin and C. A. Wight, Model-free and model-fitting approaches to kinetic analysis of isothermal and nonisothermal data, Thermochim. Acta **340-341**, 53 (1999).

[42] See Supplemental Material at http://link.aps.org/supplemental/10.1103/PhysRevMaterials.6.065404 for all models used for the the model fitting approach, the results of the model fitting approach, full colormaps of the isothermal decomposition experiments and results for the linear expansion coefficient calculated from multiple peaks.

[43] A. Khawam and D. R. Flanagan, Solid-state kinetic models: Basics and mathematical fundamentals, J. Phys. Chem. B **110**, 17315 (2006).

[44] NIST, NIST x-ray form factor, atten. scatt. tables form page https://physics.nist.gov/PhysRefData/FFast/html/form.html (2018).

[45] A. K. Galwey, What theoretical and/or chemical significance is to be attached to the magnitude of an activation energy determined for a solid-state decomposition?, J. Therm. Anal. Calorim. **86**, 267 (2006).

[46] P. Garn, Kinetics of decomposition of the solid state, Thermochim. Acta **135**, 71 (1988).

[47] A. K. Galwey, Thermal reactions involving solids: A personal view of selected features of decompositions, thermal analysis and heterogeneous catalysis, J. Therm. Anal. Calorim. **142**, 1123 (2020).

[48] B. V. L'vov, The physical approach to the interpretation of the kinetics and mechanisms of thermal decomposition of solids: The state of the art, Thermochim. Acta **373**, 97 (2001).

[49] B. V. L'vov, *Thermal Decomposition of Solids and Melts* (Springer Netherlands, Dordrecht, 2007).

[50] B. V. L'vov and A. K. Galwey, Toward a general theory of heterogeneous reactions, J. Therm. Anal. Calorim. **113**, 561 (2013).

[51] H. F. Cordes, Preexponential factors for solid-state thermal decomposition, J. Phys. Chem. **72**, 2185 (1968).

[52] T. Zhang, X. Meng, Y. Bai, S. Xiao, C. Hu, Y. Yang, H. Chen, and S. Yang, Profiling the organic cation-dependent degradation of organolead halide perovskite solar cells, J. Mater. Chem. A **5**, 1103 (2017).

[53] A. Oranskaia and U. Schwingenschlögl, Suppressing x-migrations and enhancing the phase stability of cubic $FAPbX_3$ (X = Br, I), Adv. Energy Mater. **9**, 1901411 (2019).